Front. Mech. Eng. 2023, 18(3): 47
https://doi.org/10.1007/s11465-023-0763-1

RESEARCH ARTICLE

Radial electromagnetic type unbalance vibration self-recovery regulation system for high-end grinding machine spindles

Xin PAN[a], Haoyu ZHANG[a], Jinji GAO (✉)[a], Congcong XU[a], Dongya LI[b]

[a] *Beijing Key Laboratory of Health Monitoring and Self-recovery for High-end Mechanical Equipment, Beijing University of Chemical Technology, Beijing 100029, China*
[b] *Luoyang Bearing Research Institute Corporation, Luoyang 471033, China*
✉ *Corresponding author. E-mail: gaojinji@263.net (Jinji GAO)*

© Higher Education Press 2023

ABSTRACT Modern rotating machines, which are represented by high-end grinding machines, have developed toward high precision, intelligence, and high durability in recent years. As the core components of grinding machine spindles, grinding wheels greatly affect the vibration level during operation. The unbalance vibration self-recovery regulation (UVSRR) system is proposed to suppress the vibration of grinding wheels during workpiece processing, eliminating or minimizing the imbalance. First, technical principles and the system composition are introduced. Second, the balancing actuator in the UVSRR system is analyzed in detail. The advanced nature of the improved structure is presented through structure introduction and advantage analysis. The performance of the balancing actuator is mutually verified by the theoretical calculation of torque and software simulation. Results show that the self-locking torque satisfies the actual demand, and the driving torque is increased by 1.73 times compared with the traditional structure. Finally, the engineering application value of the UVSRR system is verified by laboratory performance comparison and actual factory application. The balancing speed and effect of the UVSRR system are better than those of an international mainstream product and, the quality of the workpieces machined in the factory improved by 40%.

KEYWORDS UVSRR system, radial electromagnetic type, vibration suppression, performance simulation, engineering application

1 Introduction

High precision, intelligence, and high durability are the development direction of modern rotating machines, and the vibration suppression requirements of rotating machines are continuously increasing [1–4]. The vibration caused by spindle imbalance is one of the major faults of rotating machines and often the first problem to be investigated in engineering practice [5–7]. In the case of high-end grinding machines, grinding wheels are dynamically balanced before operation. However, factors such as the uneven abrasion of grinding wheels during the working process can lead to unevenness of the grinding wheel. Uneveness of the grinding wheel can lead to excessive spindle vibration, equipment shaking, and reduced operating accuracy. Severe cases can lead to undesirable consequences, such as breaks in operation for maintenance, safety hazards, and economic losses [8,9]. Factors such as the uneven abrasion of grinding wheels are normal phenomena that cannot be avoided when machining workpieces. Therefore, the unbalance vibration self-recovery regulation (UVSRR) of grinding machine spindles should be performed in real time during operation [10,11].

The principle of UVSRR was first proposed by the academic leader of the authors' team (Jinji GAO) at the "International Conference on Intelligent Maintenance 2003" [12]. In this principle, machines are provided with the self-recovery functions of humans to achieve the self-suppression of abnormal conditions during operation [13]. With the progress of modern science and technology and the improvement of intelligence levels, the concept of self-recovery has been recognized in domestic and foreign aviation, aerospace, petrochemical, and other

Received February 8, 2023; accepted June 13, 2023

fields [14]. The University of Illinois proposed a self-recovery rubber-toughened epoxy adhesive that can be cured at high temperatures to increase the autonomous repair capability of spacecraft structures [15]. In 2015, Casavola et al. [16] enhanced the automatic regulation capabilities of aerospace control systems after faults by combining fault diagnosis and fault-tolerant control. Li et al. [17] of Northeastern University (China) proposed abnormal operating conditions identification technology and a self-recovery regulation method for electric melt magnesium furnaces. Chen et al. [18] proposed a self-recovery regulation method for complex faults in helicopters on the basis of quantum control technologies and adaptive compensators. The authors and their team have been devoted to studying self-recovery regulation and control technology for high-end modern rotating machines in recent years. They have achieved developments in grinding wheels vibration self-recovery regulation, compressor shaft displacement faults self-recovery regulation, and turbine unit destabilization faults self-recovery regulation [19–21].

UVSRR, also known as online active balancing method [22,23], refers to the adjustment of the internal mass distribution of the balancing actuator to complete the unbalance correction of spindles without stopping rotating machines. As final execution devices, actuators have various forms, such as mechanical [24–26], hydraulic [27–29], and electromagnetic types [30–32]. Among them, electromagnetic online active balancing actuators, a new variety of online active balancing actuators, dominate in rapid action, high precision, and high durability. They have gradually become the main study direction in the field of online active balancing in domestic and foreign research. The related products mainly come from the United States, Germany, Italy, and other associated countries [33–35]. Zhejiang University, Xi'an Jiaotong University, and other universities in China have made outstanding achievements in this field [30,36,37]. However, the structures of balancing actuators studied at home and abroad are all axial electromagnetic types, which have practical problems, such as a small balance capacity and insufficient reliability. These actuators are not conducive to engineering application and promotion. Since 2009, the authors' team has conducted continuous improvement research on this problem and innovatively proposed the radial electromagnetic structure of balancing actuators. The structure was granted Chinese and American invention patents and has been applied in engineering practice, achieving practical application in many enterprises [38].

To address the unbalanced vibration problem of high-end grinding machine spindles, a radial electromagnetic type UVSRR system is proposed in this paper. In Section 2, the principle of the UVSRR method and the composition of the UVSRR system are introduced. In Section 3, the structure and the driving principle are presented, and the analysis of the performance calculation and the simulation of the radial electromagnetic type online active balancing actuator is discussed. In Section 4, the performance of the balancing actuator and the UVSRR system are verified on a grinding machine test bench and in the practical application on a high-end grinding machine. Finally, the conclusions and the future research direction are presented in Section 5.

2 Radial electromagnetic type UVSRR system

2.1 Principle of the UVSRR method

The UVSRR method can eliminate or minimize vibration in real time during the operation of equipment by applying the fault self-recovery principle. On the basis of "molecular targeting therapy" in contemporary medical science, the UVSRR method can diagnose and predict the cause and condition of faults in real time, determine the target, and apply self-recovery force to change the rotor mass distribution to suppress the vibration fault through intelligent decision-making.

The mainstream control method commonly used in automatic balancing systems at present is the optimization-seeking method. The optimization-seeking process requires phase optimization and then amplitude optimization until the vibration amplitude of the equipment is reduced to below the set value. By contrast, the control command of the UVSRR method has a clear directional and quantitative value, like target shooting, and the control speed is high. This method effectively avoids the occurrence of misalignment and overshoot, and the vibration amplitude monotonically decreases during the control process.

The vibration differential equation of the spindle system can be written as Eq. (1):

$$\boldsymbol{M}\ddot{\boldsymbol{x}} + (\boldsymbol{C} + \omega\boldsymbol{G})\dot{\boldsymbol{x}} + \boldsymbol{K}\boldsymbol{x} = \boldsymbol{F}_0\cos(\omega t + \boldsymbol{\varphi}), \tag{1}$$

where $\boldsymbol{M}$ is the mass matrix, $\boldsymbol{C}$ is the damping matrix, $\boldsymbol{G}$ is the gyroscopic matrix, $\boldsymbol{K}$ is the stiffness matrix, $\boldsymbol{\omega}$ is the angular velocity, t is time, $\boldsymbol{\varphi}$ is the initial phase, $\boldsymbol{x}$ is the vibration parameter of amplitude and phase, and $\ddot{\boldsymbol{x}}$ is the second derivative of amplitude with respect to time and the acceleration of the spindle system. The unbalanced fault force on the spindle system is $\boldsymbol{F}_0$, so the vibration amplitude of the spindle system can be written as Eq. (2):

$$\boldsymbol{x} = \frac{\boldsymbol{F}_0}{\sqrt{(\boldsymbol{K} - \boldsymbol{M}\omega^2)^2 + (\boldsymbol{C} + \omega\boldsymbol{G})^2\omega^2}}. \tag{2}$$

For the UVSRR method, an online active balancing actuator that rotates simultaneously with a spindle must be pre-installed. If the mass matrix of the balancing actuator is $\boldsymbol{m}$ and the resultant self-recovery force is $\boldsymbol{F}_1$, then the vibration differential equation of the spindle system can be rewritten as Eq. (3):

$$(\boldsymbol{M}+\boldsymbol{m})\ddot{\boldsymbol{x}}+(\boldsymbol{C}+\omega\boldsymbol{G})\dot{\boldsymbol{x}}+\boldsymbol{K}\boldsymbol{x}=(\boldsymbol{F}_0-\boldsymbol{F}_1)\cos(\omega t+\varphi). \quad (3)$$

When the balancing actuator of the UVSRR system adjusts the mass distribution by adjusting the phase distribution of the counterweight discs with a definite target, self-recovery force $\boldsymbol{F}_1$ can gradually offset the system's own unbalance fault force $\boldsymbol{F}_0$. The vibration amplitude of the spindle system decreases to a permissible range when the two forces are nearly equivalent in size and opposite in direction.

2.2 Composition of the UVSRR system

The UVSRR system mainly consists of a control device, a power device, a balancing actuator, sensors, and other accessories.

The working principle of the UVSRR system is shown in Fig. 1. A vibration acceleration sensor, a photoelectric speed sensor, and hall sensors are used to measure the vibration and speed signals of the spindle and the phase signals of two counterweight discs. Then, the above signals are used as input to the data acquisition module simultaneously of the control device. The data acquisition module performs real-time signal processing. After receiving the vibration parameters of the spindle system, the control device quickly locates the initial vibration amplitude of the spindle system using the UVSRR method. Then, a control command is formed to instruct the balancing actuator. According to the control command, the power device will generate a corresponding electrical signal, which will cause a magnetic field inside the balancing actuator and drive the counterweight discs of the balancing actuator through electromagnetic force. The counterweight discs rotate step by step toward the target position, generating a vector that can gradually offset the initial vibration of the spindle system for the amplitude to progressively decrease. When both counterweight discs reach the target position, the compensation vector generated by the counterweight blocks is approximately equal in size and opposite in direction to the initial unbalance vector of the spindle system. The vibration amplitude reaches a lower level, and the UVSRR process ends.

3 Radial electromagnetic type online active balancing actuator

3.1 Structure and driving principle of the balancing actuator

The radial electromagnetic type of online active balancing

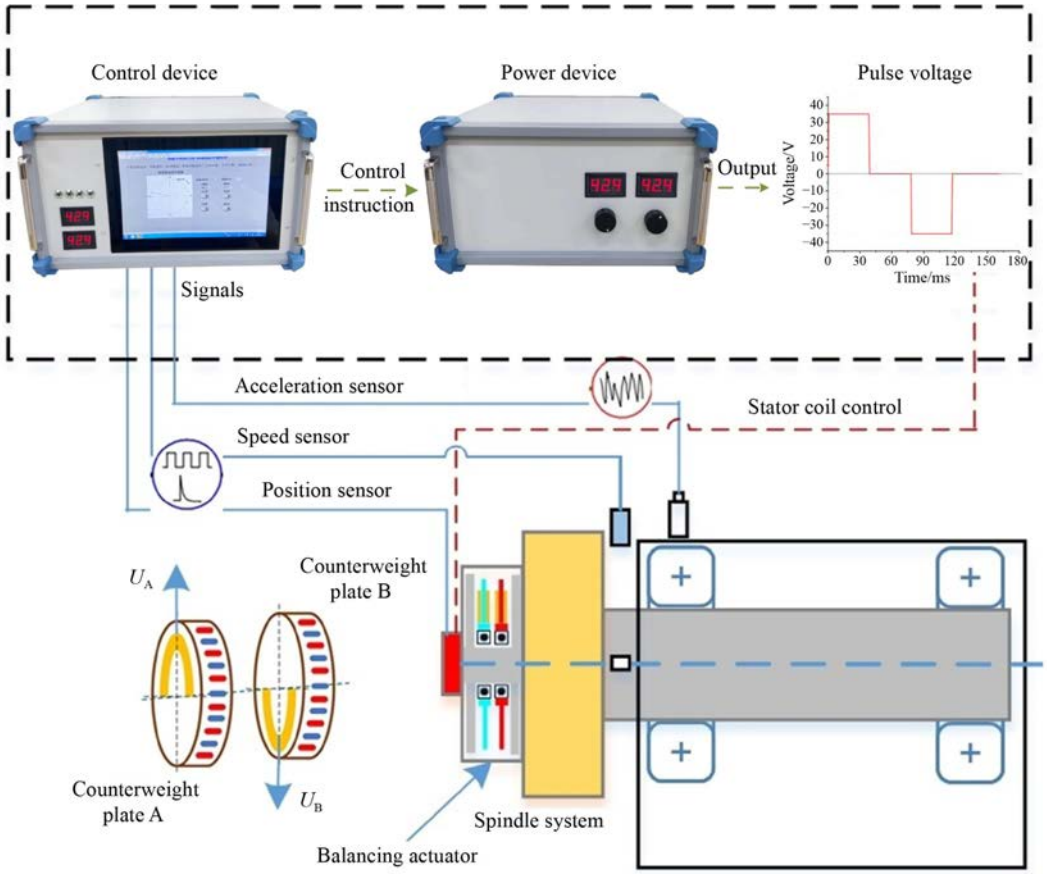

Fig. 1 Composition of unbalance vibration self-recovery regulation system.

actuator mainly consists of a rotating part and a stationary part, and the structure is symmetrical. The rotating part rotates with the spindle system, while the stationary part is fixed and does not rotate. Bearings are installed between the rotating and stationary parts to ensure relative rotation.

The rotating part of the balancing actuator includes an aluminum shell, two outer excitation rings, two inner excitation rings, two counterweight discs with counterweight blocks, and corresponding fasteners. The "radial electromagnetic type" in the name of the balancing actuator means that the counterweight disc adds a convex ring structure to the outer circumference of the traditional disc and installs magnets and soft irons in the convex ring, as shown in Fig. 2(e). The convex ring is installed in the gap between the two excitation rings. Thus, the inner excitation ring teeth, the magnets and soft irons, and the outer excitation ring teeth are arranged in the radial direction in the balancing actuator. The magnetic induction lines generated in the structure after excitation are arranged in the radial direction, which is why the excitation structure used in the balancing actuator is called a "radial electromagnetic" structure.

The stationary part of the balancing actuator includes a central stator, two excitation bobbins, two coils, an aerial plug holder, and corresponding fasteners. The coils are installed in the excitation bobbins and are led from the axial direction on both sides. The coil near the connection flange side is passed to the other side through the central stator through hole, and the coils on both sides converge and are connected to the aerial plug. The aerial plug holder integrates the hall sensor and coil conductors.

The balancing actuator is fixed to the end of the connection flange through the aluminum shell. The other end of the connection flange is set to the end of the spindle system so that the balancing actuator can rotate together with the spindle. The stationary part is immovable and receives an electrical signal from the power device, which is fed with an alternating voltage. And the coils generate alternating magnetic fields to drive the counterweight discs to compensation position by electromagnetic force, as shown in Fig. 3. The counterweight blocks on the counterweight discs generate a compensating vector to correct the imbalance.

The counterweight discs are symmetrically embedded with magnets and soft irons, with adjacent magnets of opposite polarity at the same end. The magnetic attraction force between the magnets and the excitation rings ensures that the counterweight discs are self-locking state. When a magnetic field is applied, electromagnetic force can drive the movement of the counterweight discs. The soft irons increase the driving torque without affecting the self-locking torque to drive the counterweight discs with high efficiency. Taking one of the counterweight discs as an example, when no power is applied, the counterweight disc relies on the magnetic attraction force to maintain the self-locking state, as shown in Fig. 3(a). After applying a pulse driving voltage, the coil is energized to produce a

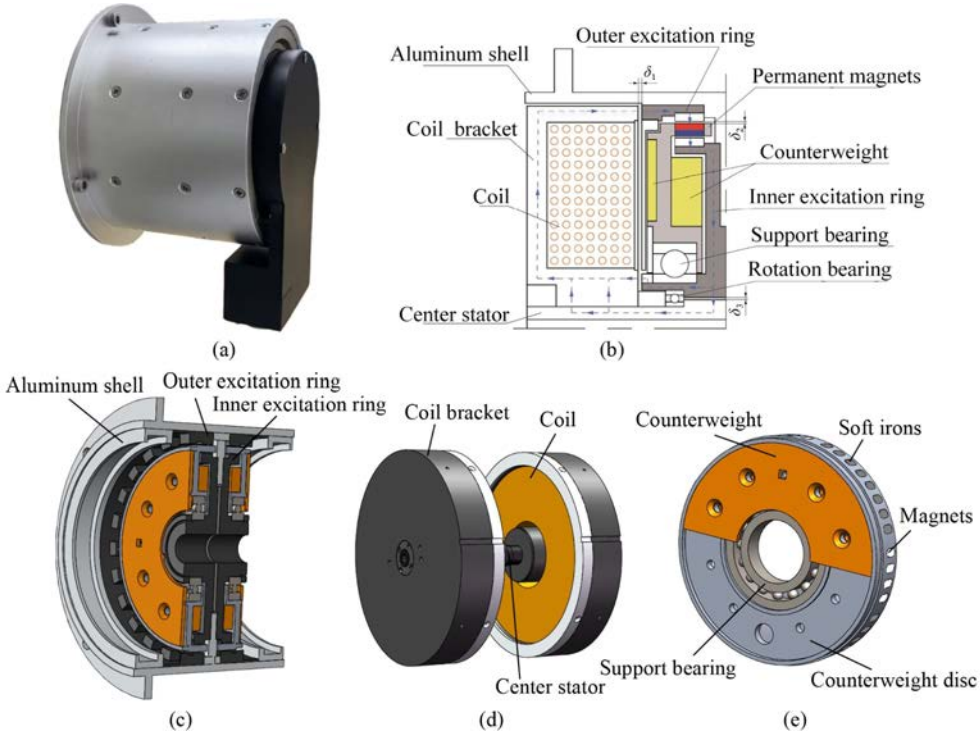

Fig. 2 Structure of the balancing actuator: (a) overall structure, (b) cross-sectional view, (c) rotating part, (d) stationary part, and (e) counterweight disc.

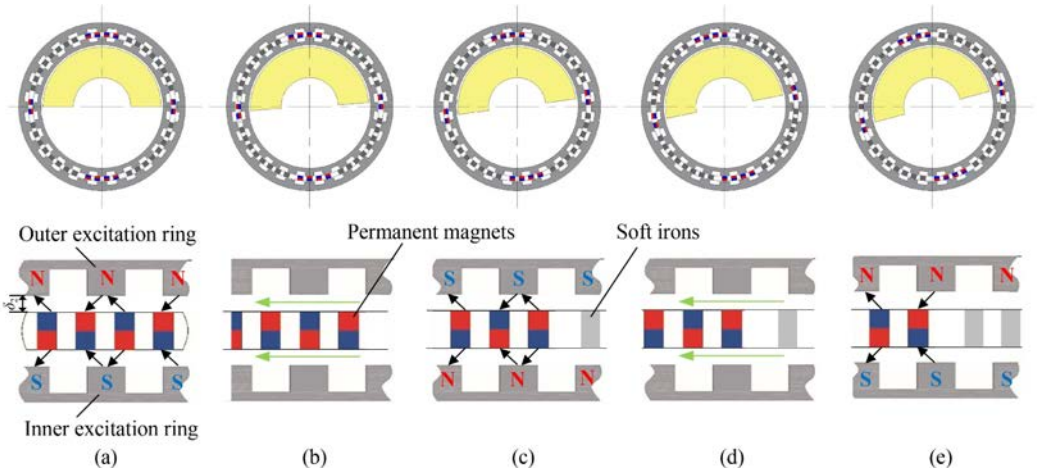

Fig. 3 Drive principle of counterweight discs: (a) self-locking position, (b) middle position, (c) next self-locking position, (d) next middle position, and (e) following self-locking position.

magnetic field. The coil magnetizes the excitation rings made of soft irons, and the magnetized poles are shown in Fig. 3(a). According to the principle of the same poles repelling and opposite poles attracting, as shown by the arrow in Fig. 3(b), the counterweight disc is subjected an electromagnetic force and starts to move to the left toward the position shown in Fig. 3(b). At this time, the coil is disconnected, and the magnetic field disappears. Then, the counterweight disc relies on inertia and its speed to reach the next stable self-locking position. If the counterweight disc must continue to rotate in the same direction, then an opposite pulse driving voltage must be applied to generate an opposing magnetic field because the magnet's polarity in the same position changes compared to that earlier, as shown in Figs. 3(c)–3(e). The power device repeatedly applies forward and reverse pulse drive voltages, which enable the counterweight disc to continuously overstep until it reaches the target position.

3.2 Advantages of the "radial electromagnetic" structure

Figure 4 shows the comparison of the "radial electromagnetic" and "axial electromagnetic" structures, with the "axial electromagnetic" structure on the left and the "radial electromagnetic" structure on the right in each part. The improvement points of the "radial electromagnetic" structure are as follows:

1) The structural dimensions between the excitation components are different. The "radial electromagnetic" structure is a nested structure, so the corresponding components have gradually decreased outer diameters. By contrast, the "axial electromagnetic" structure is a parallel structure, and the corresponding components have the same outer diameters, as shown in Fig. 4(a).

2) The shapes of the counterweight discs are different. On one hand, the counterweight disc in the "radial electromagnetic" structure adds a convex ring structure to the outer circumference of the traditional disc, and magnets and soft irons are installed in the convex ring. On the other hand, the "axial electromagnetic" structure is a traditional disc, as shown in Fig. 4(c).

3) The number and distribution of magnets and soft irons on the counterweight discs are different. The "radial electromagnetic" structure adopts the high efficiency driving technology of combined magnets and soft irons. The soft irons can provide the driving torque for balancing the actuator without affecting the self-locking torque, improving the driving efficiency. By contrast, the "axial electromagnetic" structure must be driven by full magnets to meet the working requirements due to the large air gap between its excitation components.

The advantages brought by these improvement points are as follows. (1) The magnetic field transfer direction is changed, as shown by the yellow arrows in Fig. 4(b). The force direction is changed from axial to radial, which increases the stability of the balancing actuator. In the traditional "axial electromagnetic" structure, counterweight discs are subjected to axial electromagnetic force. Furthermore, when an external magnetic field is applied, the excitation components may falter or even collide in the axial direction under the influence of the magnetic attraction and electromagnetic forces, significantly affecting the stability of the balancing actuator. If the air gap between the excitation components increases to avoid touching and friction, the magnetic permeability and the driving efficiency will be reduced. However, the "radial electromagnetic" structure changes the direction of the magnetic attraction and electromagnetic forces on the counterweight discs from axial to radial through the nested installation of the excitation components. And the axial center is fixed, so the excitation components cannot be radially tampered, improving the operation stability. (2) The air gap between the excitation components is greatly reduced, the efficiency of magnetic field transmission is improved, and the self-locking torque and the

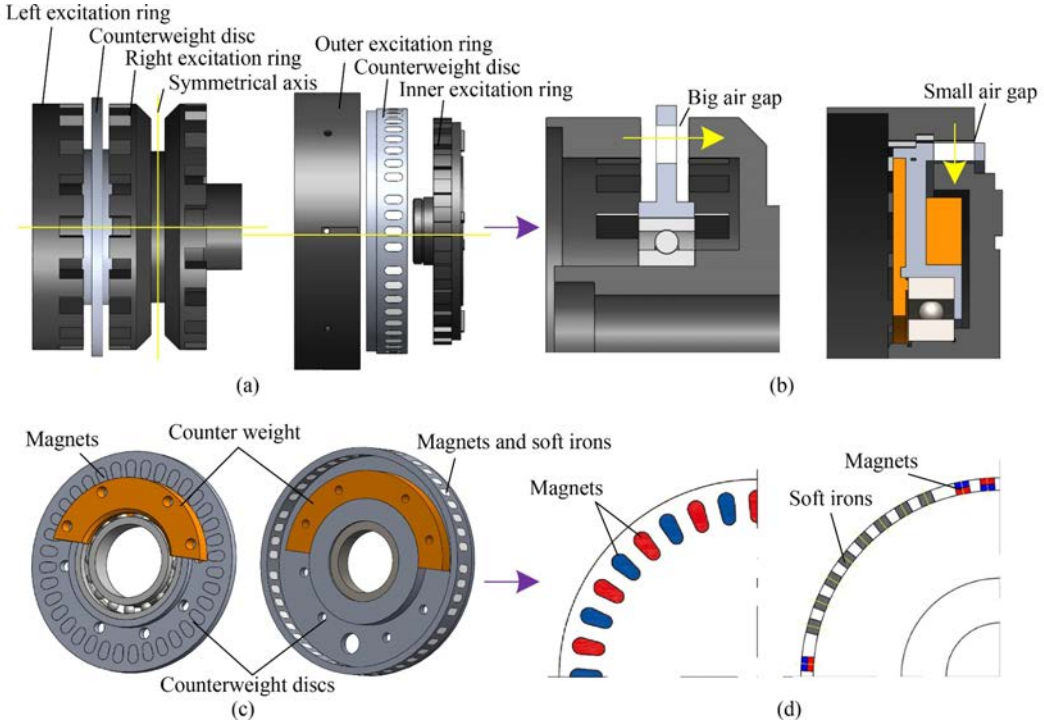

Fig. 4 Advantages analysis of the "radial electromagnetic" structure: (a) excitation components, (b) directions of magnetic field transfer, (c) models of different counterweight discs, and (d) arrangements of magnets and soft irons.

driving efficiency are enhanced. Given the change in excitation method, the stability of the excitation components is improved, and the air gap between them can be exponentially reduced. The magnetic attraction force between the excitation components increases, so the self-locking torque increases. More importantly, fewer magnets are needed to meet the required self-locking torque. Soft irons are installed symmetrically along the circumference in the remaining holes of the counterweight disc, providing additional driving torque while ensuring a uniform radial force on the counterweight disc to ensure structural stability. The high efficiency driving technology of combined magnets and soft irons increases the drive torque further and improves the drive efficiency without affecting the self-locking torque.

3.3 Analysis of self-locking performance

The radial electromagnetic type online active balancing actuator is selected as the final execution device of the UVSRR system, and its performance directly affects the control level of the UVSRR system. In turn, the control level of the UVSRR system determines the vibration level of high-end grinding machine spindles. The counterweight discs rely on the magnetic attraction force to maintain stable self-locking at each balancing position. Theoretical calculations and software simulations of the self-locking torque are performed to verify its reliability.

3.3.1 Calculation of self-locking torque

When the ratio of air gap δ_2 between the excitation components to the radius of the magnet R_g does not exceed 1, the attraction force between the magnets ($\boldsymbol{F}_g$) can be calculated by Eq. (4):

$$\boldsymbol{F}_g = \frac{1}{2\mu_0} A_g \boldsymbol{B}_g^2, \tag{4}$$

where μ_0 denotes the magnetic permeability of air, A_g is the effective magnetic pole area, and $\boldsymbol{B}_g$ is the magnetic induction intensity generated by the magnets. Magnetic density $\boldsymbol{B}_g$ can be expressed as Eq. (5):

$$\boldsymbol{B}_g = \frac{\boldsymbol{B}_r}{2}\left(1 - \frac{\delta_2}{\sqrt{\delta_2^2 + R_g^2}}\right), \tag{5}$$

where $\boldsymbol{B}_r$ is the remaining magnetic strength of the magnets. Thus, total self-locking force $\boldsymbol{F}$ and total self-locking torque $\boldsymbol{T}_s$ can be expressed as Eqs. (6) and (7):

$$\boldsymbol{F} = K\boldsymbol{F}_g = \frac{K}{8\mu_0} A_g \boldsymbol{B}_r^2 \left(1 - \frac{\delta_2}{\sqrt{\delta_2^2 + R_g^2}}\right)^2, \tag{6}$$

$$\boldsymbol{T}_s = \boldsymbol{F}R = \frac{K}{8\mu_0} R A_g \boldsymbol{B}_r^2 \left(1 - \frac{\delta_2}{\sqrt{\delta_2^2 + R_g^2}}\right)^2, \tag{7}$$

where K is the number of magnets, and R is the mounting radius of the magnets. The specific values of the parameters and the results are shown in Tables 1 and 2, respectively.

The balancing actuator requires the counterweight discs to maintain self-locking and follow the synchronous rotation of the rotating part when no power signal is received. If the counterweight discs cannot maintain self-locking, the phase constantly changes. This phenomenon will cause great unevenness, preventing the counterweight discs from moving accurately to reduce the vibration of the grinding machine spindles. The accuracy of the self-locking torque value is obtained through calculation. To determine whether this value can meet the actual self-locking requirement, the minimum self-locking torque for the balancing actuator operation is analyzed and calculated to verify the self-locking performance. The minimum self-locking torque ($\boldsymbol{T}_{\mathrm{sm}}$) required for the balancing actuator can be determined by Eq. (8):

$$\boldsymbol{T}_{\mathrm{sm}} = K_{\mathrm{sf}}\left(J\boldsymbol{\alpha} + m_1\boldsymbol{g}R_1 + m_2\boldsymbol{g}R_2\right), \tag{8}$$

where K_{sf} is the safety factor, J is the rotational inertia of the counterweight discs and its accessories, $\boldsymbol{\alpha}$ is the spindle starting acceleration, $\boldsymbol{g}$ is the gravitational acceleration, and m_1, m_2, R_1, and R_2 are the mass and the center of gravity of the counterweight blocks. The specific values of the parameters are shown in Table 3.

The required minimum self-locking torque for a safety factor of 2 is compared with the actual minimum self-locking torque for a safety factor of 1. A safety factor of 2 ensures that the counterweight disc maintains self-locking in the event of an accident, such as a bump, and prevents the counterweight disc from rotating in a disorderly manner that would cause additional imbalance in the entire system. Taking the safety factor of 2 as an example and using the relevant data of the actuator for calculation, the minimum self-locking torque value ($\boldsymbol{T}_{\mathrm{sm}}$) for the stable operation of the actuator is 155 mN·m. The designed self-locking torque exceeds this value and meets the functional requirements.

Table 1 Parameters related to design self-locking torque

Parameter	Value
Magnet material	NdFe35
Air gap δ_2	0.5 mm
Magnet radius R_{g}	3 mm
Magnetic permeability of free space μ_0	$4\pi \times 10^{-7}$ H/m
Effective magnetic pole area A_{g}	12.85 mm^2
Remaining magnetic strength $\boldsymbol{B}_{\mathrm{r}}$	1.09 T
Magnet number K	12
Magnet mounting radius R	52.25 mm

Table 2 Calculation results of design self-locking torque

Result	Value
Single magnet self-locking force $\boldsymbol{F}_{\mathrm{g}}$	1.258 N
Magnetic induction intensity $\boldsymbol{B}_{\mathrm{g}}$	0.496 T
Total self-locking force $\boldsymbol{F}$	15.09 N
Total self-locking torque $\boldsymbol{T}_{\mathrm{s}}$	788.4 mN·m

Table 3 Parameters related to minimum self-locking torque

Parameter	Value
Safety factor K_{sf}	2
Rotational inertia of the counterweight discs and its accessories J	8.08×10^5 g·mm^2
Rotor starting acceleration $\boldsymbol{\alpha}$	52.4 rad/s^2
Mass of internal counterweight block m_1	85.5 g
Center of gravity of internal counterweight block R_1	23.56 mm
Mass of external counterweight block m_2	65.7 g
Center of gravity of external counterweight block R_2	24 mm

3.3.2 Simulation of self-locking torque

The designed self-locking torque was calculated to be 788.4 mN·m. The electromagnetic analysis software Ansys Maxwell is used in self-locking torque simulations to verify the correctness of the designed self-locking torque value.

The actuator model and the simulation results are shown in Fig. 5. The parameters are set as follows. The soft iron material, such as the inner and outer excitation rings, is DT4C. The magnetic material is NdFe35, with remaining magnetic strength $\boldsymbol{B}_{\mathrm{r}}$ = 1.09 T, and magnetic coercivity H_{c} = 890 kA/m. Non-magnetic materials, such as air and aluminum, have a relative permeability of μ = 1.0, and bearing steel has a relative permeability of μ = 200. The simulation parameters of the materials are set similarly as the actual materials. The counterweight disc rotates from the initial balancing position to the following balancing position, and the moment applied to the counterweight disc during the rotation is analyzed.

The orange curve in Fig. 6 shows the self-locking torque curve simulated for an air gap of 0.5 mm between the excitation components, with the maximum torque of 772 and −797 mN·m. The error is within 3% compared with the designed self-locking torque value of 788.4 mN·m, so the conclusion is reliable. Figure 5(c) shows the magnetic induction lines at the initial self-locking state, and the magnets and the excitation rings are enough to form a self-closing circuit to complete the self-locking. Figure 5(d) shows the magnetic induction lines after rotating by 3.75°. The magnets rotate to the middle of the excitation ring teeth and are simultaneously subjected to the left and right magnetic attraction force and cancel out, so the torque is 0. The second half of the torque analysis is the same as the first half. The calculated values' correctness is verified through software simulation, and the self-locking law is derived.

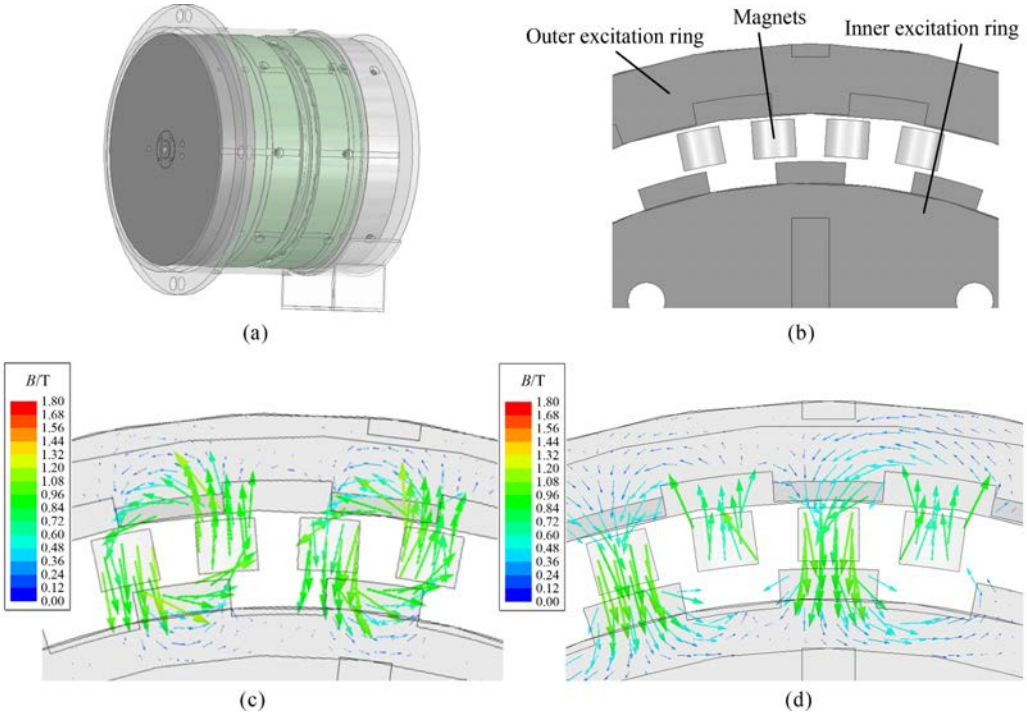

Fig. 5 Simulation model and animations of self-locking torque: (a) electromagnetic simulation model of balancing actuator, (b) electromagnetic simulation model of excitation components, (c) self-locking simulation result one, and (d) self-locking simulation result two.

The green curve in Fig. 6 shows the self-locking torque simulated for an air gap of 1.0 mm between the excitation components, with the maximum torque of 291 and −275 mN·m. This air gap is the gap between the excitation components of most balancing actuators with a traditional "axial electromagnetic" structure. Compared with the two excitation structures, the shape and size of the teeth of the excitation rings and the magnets on the counterweight discs are the same. Only the transmission direction of the magnetic induction lines and the air gap between the excitation components are different, so the 1.0 mm gap can accurately simulate the axial excitation structure. The maximum self-locking torque of the "radial electromagnetic" structure is 2.65 times higher than that of the "axial electromagnetic" structure because the "radial electromagnetic" structure can meet the minimal air gap between the excitation components, which enhances the magnetic attraction force and increases the self-locking torque. In addition, the increased magnetic attraction force also positively affects the driving torque, as discussed in the following sections.

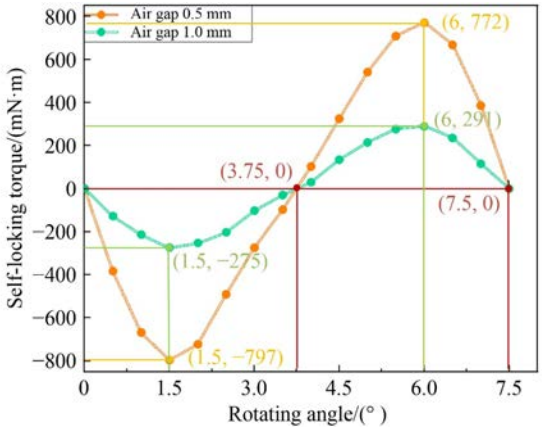

Fig. 6 Simulation results of self-locking torque.

3.4 Analysis of drive performance

The electromagnetic analysis software Maxwell is used to analyze the driving torque performance, and the parameter settings are the same as those in the self-locking torque analysis. The simulation explores the phase of an individual magnet in continuous stepwise movement and the torque on the counterweight discs. The counterweight disc is continuously moved stepwise by applying pulse voltages to the balancing actuator. The applied pulse voltage is shown in Fig. 7(a) and the magnet rotation angle is shown in Fig. 7(b). The animation of the individual magnet's stepwise movement on the counterweight disc is shown in Fig. 8.

Current is applied to the left coil, and the model permeability and the magnetic induction intensity distribution are observed. Figure 9 shows the simulation results analyzed by the electromagnetic analysis software Maxwell. Figure 9(a) shows the simulation model's

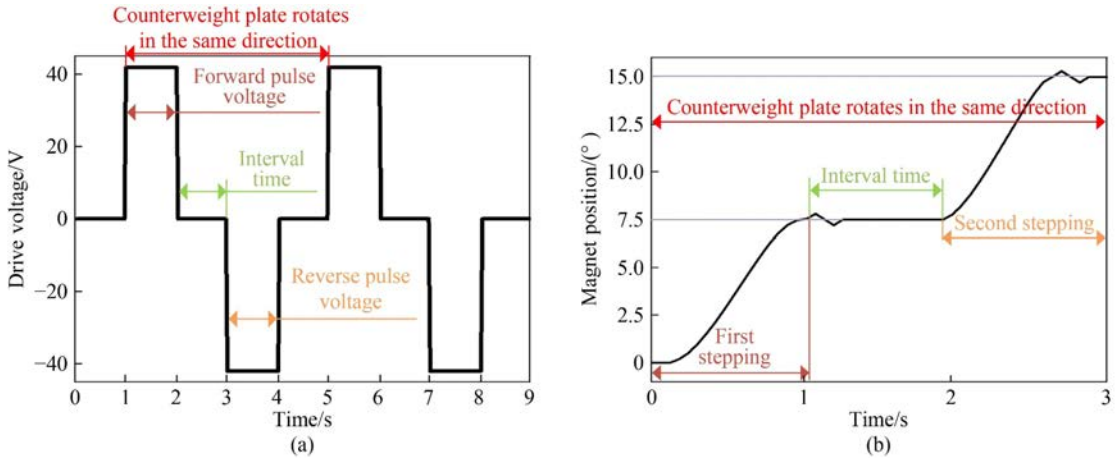

Fig. 7 Simulation waveforms of drive performance: (a) waveform of drive voltage and (b) rotation angle of counterweight disc.

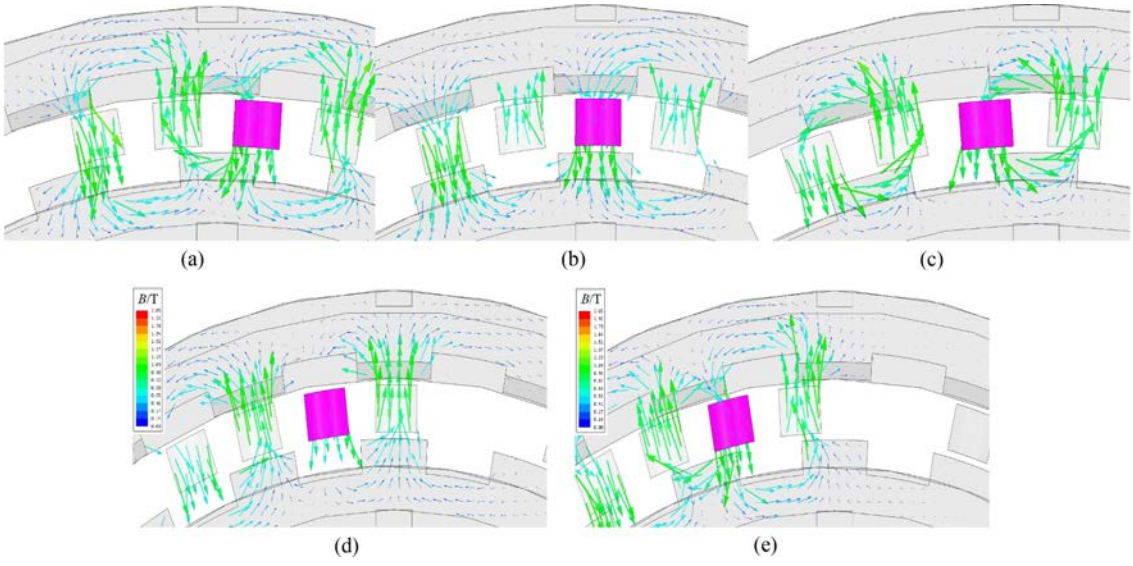

Fig. 8 Continuous stepping animations of counterweight disc: (a) starting position (0°), (b) middle position (3.75°), (c) self-locking position (7.5°), (d) next middle position (11.25°), and (e) next self-locking position (15°).

magnetic induction lines of the radial electromagnetic structure, which are closed enough along the magnetic circuit to form a complete circuit. An enlarged view of the simulation results of the magnetic induction lines at the two air gaps is shown in Fig. 9(a). The results are shown in the orange box in Fig. 9(a). The magnetic induction lines at the two air gaps are coherent and shows good permeability, with only a very small leakage part. Figure 9(b) shows the simulation model of the axial electromagnetic structure and the trend of the magnetic induction lines. The simulation model is identical to the actual actuator, and the gap between the excitation components is 1 mm, whereas the gap between the excitation components of the radial excitation structure is 0.5 mm.

Figure 9(c) shows how the driving torque varies with the number of soft irons on the counterweight discs. The driving torque increases from 2.56 to 6.62 N·m with the increase of the number of soft irons from 0 to 24, the driving torque by 2.58 times and dramatically improves the driving performance. Figure 9(d) shows the driving torque variation curves of the “radial electromagnetic structure” and “axial electromagnetic structure” during the stepping process of counterweight discs. With the radial electromagnetic structure, the gap between the excitation components is greatly reduced, resulting in an increase in drive torque from 3.83 to 6.62 N·m. The drive torque of the balancing actuator is increased by 1.73 times, and drive performance is proven. The drive performance simulation further verifies the feasibility of the balancing actuator and provides theoretical support for physical performance verification.

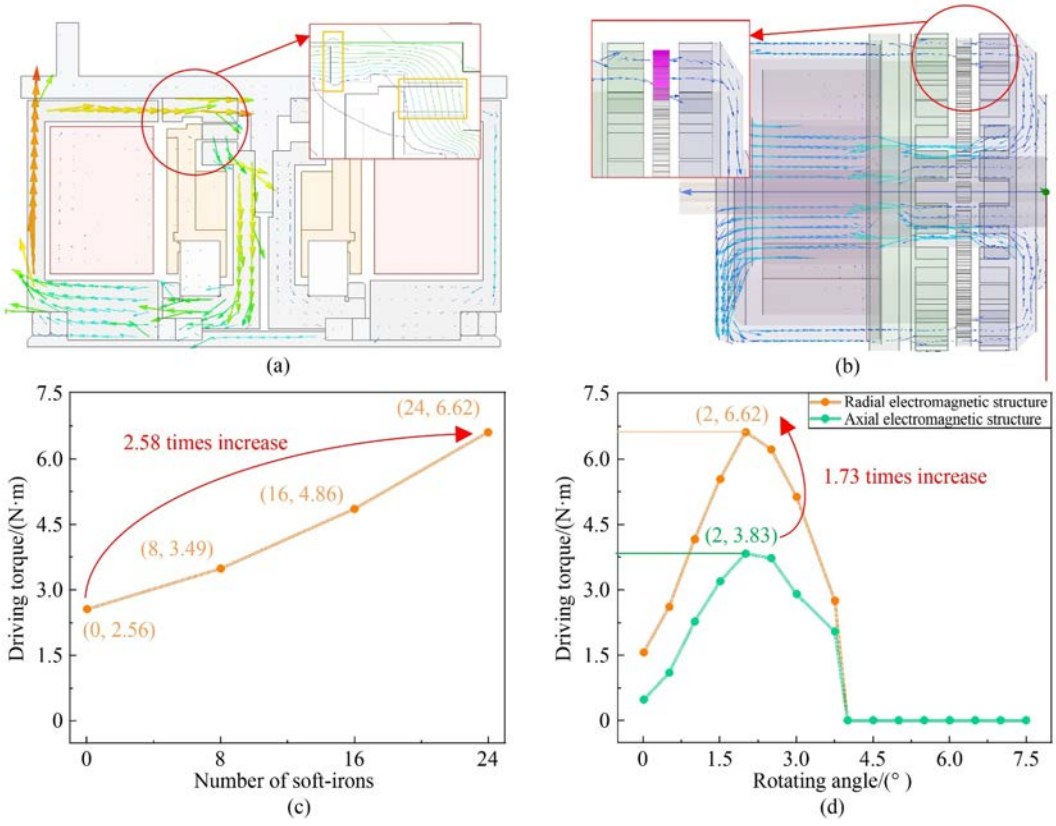

Fig. 9 Simulation results of drive performance: trend of magnetic induction lines of (a) the radial electromagnetic structure and (b) the axial electromagnetic structure, (c) variation of driving torque with the number of soft irons, and (d) drive torque curve with rotating angle.

4 Performance verification and application of UVSRR system

4.1 Performance verification of the balancing actuator and UVSRR system

A high-end grinding machine self-recovery regulation test bench was built to verify the performance of the radial electromagnetic type UVSRR system and designed with reference to a universal cylindrical grinding machine. The test bench consisted of a three-phase asynchronous motor, a spindle case, a grinding wheel, a frequency converter, a radial electromagnetic type online active balancing actuator, a control device, a power device, and sensors. The balancing actuator rotated simultaneously with the grinding wheel through the connection flange. After receiving the command, the balancing actuator drove the counterweight discs to change their mass distribution to achieve the purpose of compensation mass. The UVSRR system controller was used to monitor the amplitude and phase of the vibration and send action commands to the balancing actuator. The power supply box supplied power to the balancing actuator coils. The UVSRR system controller and the power supply box were connected to the balancing actuator through an aviation plug, as shown in Fig. 10.

The reliability of the balancing actuator was verified by the UVSRR program. The program's interface is shown in Fig. 11. After starting the grinder, the balancing actuator rotated simultaneously with the grinding wheel without applying any action. The phase of the A and B counterweight discs was detected and observed to determine whether their phase could be kept stable to verify their self-locking performance, and the experimental result is shown in Fig. 12(a). Then, the UVSRR program drove the A and B counterweight discs to rotate 360°, respectively, and was observed to determine whether a mistuning or over-tuning phenomenon occurred. The experimental result is shown in Fig. 12(b). Two experiments verified the stability and reliability of the balancing actuator.

Test weights of different masses were installed at different angles of the grinding wheel to simulate any angle and size of vibration that may occur during operation to verify the performance of the UVSRR system. The test weights of 14.8, 25.1, 35.2, and 64.5 g were individually and repeatedly installed at eight arbitrary positions on the grinding wheel in the range of 0° to 360°, and the vibration induced by the test weights

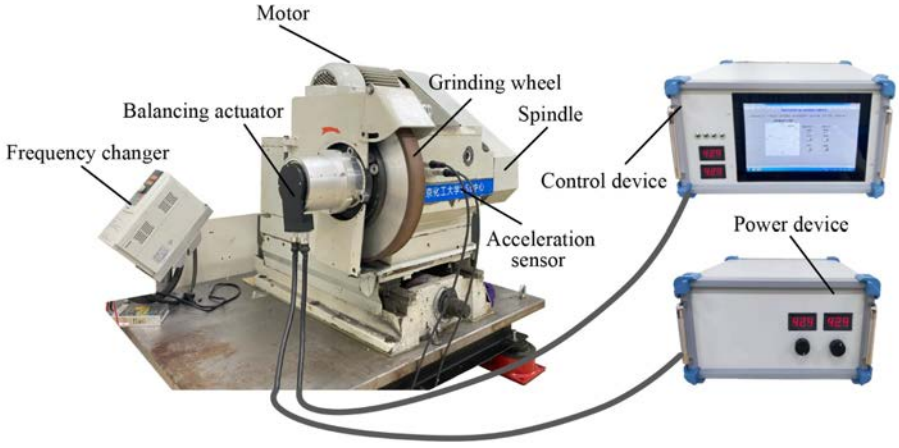

Fig. 10 High-end grinding machine self-recovery regulation test bench.

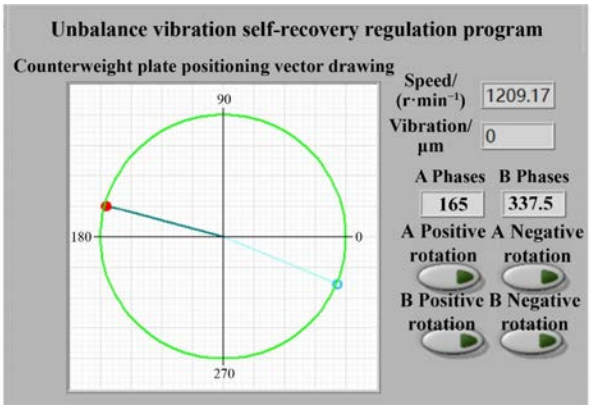

Fig. 11 Unbalance vibration self-recovery regulation program.

was suppressed by the UVSRR system. The experimental results are shown in Fig. 13. The UVSRR system described in this paper can suppress the vibration of grinding wheels of any size and direction to less than 1 μm if the vibration does not exceed the balancing capacity of the balancing actuator. This feature ensures the standard grinding work of the grinding machine and improves the machining accuracy.

The performance of the UVSRR system was further verified by comparing it with that of an international mainstream online active balancing product. The balancing actuator of the UVSRR system has a comparable balancing capacity, the same installation method, and a comparable external dimension as an international mainstream product. The only difference is in the internal structure of the balancing actuator and the driving method in the two systems. Thus, the appropriate specifications are chosen to meet the test standard. The two systems were installed separately on the high-end grinding machine test bench for vibration suppression. The vibration was excited by the test weights mounted on the grinding wheel to simulate the unbalanced vibration of the spindle. Moreover, the weight and mounting position of the test weights were precisely the same to ensure that the installed system was the only variable. The experimental results are shown in Fig. 14.

After comparison, the following conclusions were

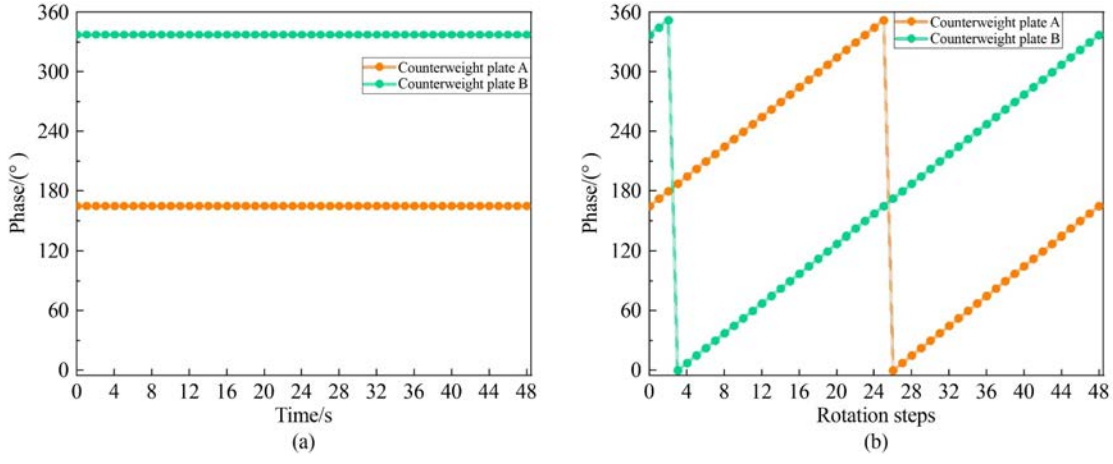

Fig. 12 Movements of counterweight discs: (a) self-locking performance experiment and (b) drive performance experiment.

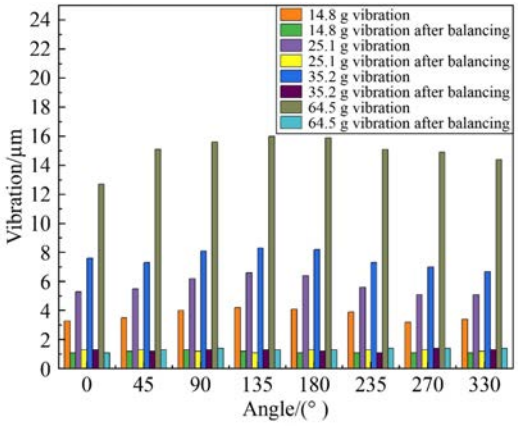

Fig. 13 Experimental results of vibration suppression of the high-end grinding machine self-recovery regulation test bench.

drawn. (1) The UVSRR system made the vibration amplitude monotonically decrease when suppressing vibration and consumed a short time, exhibiting superiority over the international mainstream online active balancing product. The international mainstream online active balancing product was mis-tuned and over-tuned in the process of vibration suppression, resulting in a sudden increase in vibration amplitude many times, which is not conducive to the safe and stable operation of the equipment. The UVSRR system adopts the UVSRR method, whose control command has clear direction and quantity, allowing the quick location of the unevenness and suppression of the vibration. (2) The final vibration suppression effect of the UVSRR system is comparable to that of the international mainstream online active balancing product. Both systems could suppress the vibration amplitude to less than 1 μm, satisfying the actual application requirements. Therefore, the UVSRR system can quickly suppress vibration and decrease the vibration amplitude monotonically. The proposed system's practicality is better than that of the international mainstream online active balancing product and more aligned with the actual application requirements.

4.2 Factory applications of UVSRR system

A universal cylindrical grinding machine in a factory was used as the experimental object, and the radial electromagnetic type UVSRR system described in this paper was installed for on-site self-recovery regulation tests and the machining of workpieces. The grinding machine speed is 1500 r/min. First, the grinding machine was used to machine a workpiece without installing the proposed system. A certain amount of unbalanced vibration was observed due to the grinding wheel wear and other reasons. The measured vibration amplitude at this time was approximately 2 μm, which is consistent with the

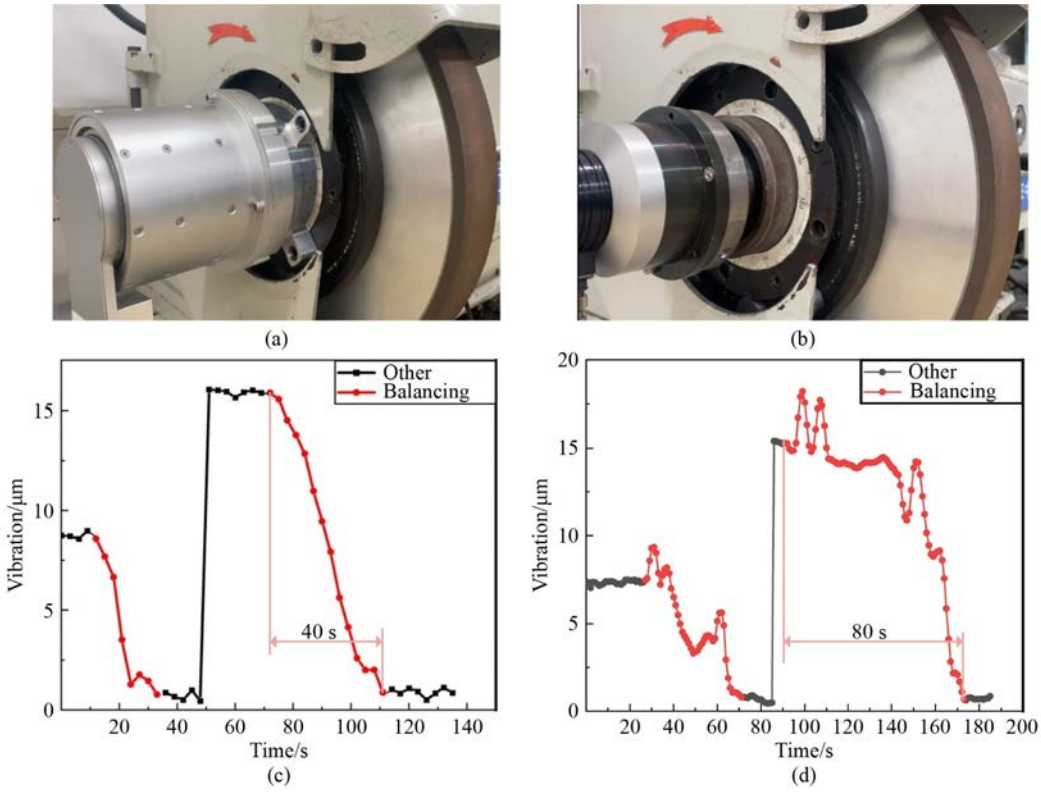

Fig. 14 Comparison of two systems: (a) unbalance vibration self-recovery regulation (UVSRR) system, (b) an international mainstream product, vibration suppression curve of (c) UVSRR system and (d) the international mainstream product.

actual production situation. Second, the grinding machine was installed with the radial electromagnetic type UVSRR system and completed the UVSRR progress. The same type of workpiece was processed again to ensure that the vibration amplitude of the grinding machine was the only variable. Figure 15 shows the site photo of the cylindrical grinding machine with the radial electromagnetic type UVSRR system. Figure 16(d) shows the vibration reduction curve of the UVSRR system. The initial vibration amplitude of the grinding machine was 4.6 μm, and the vibration amplitude of the grinding machine was reduced to approximately 0.4 μm in 20 s with the UVSRR system, and the amplitude reduction ratio was as high as 91.3%.

On the basis of the universal cylindrical grinding machine, several different workpieces were ground and machined separately. After machining, the parameters of the machined workpieces, such as size, roundness, cylindricity, roughness, and shape error, were tested and compared using a professional coordinate inspection instrument, as shown in Table 4. The test results show that vibration greatly influenced the roundness and shape error of the machined workpieces. After the vibration suppression by the UVSRR system, the surface quality of

Fig. 15 A universal cylindrical grinding machine with unbalance vibration self-recovery regulation system.

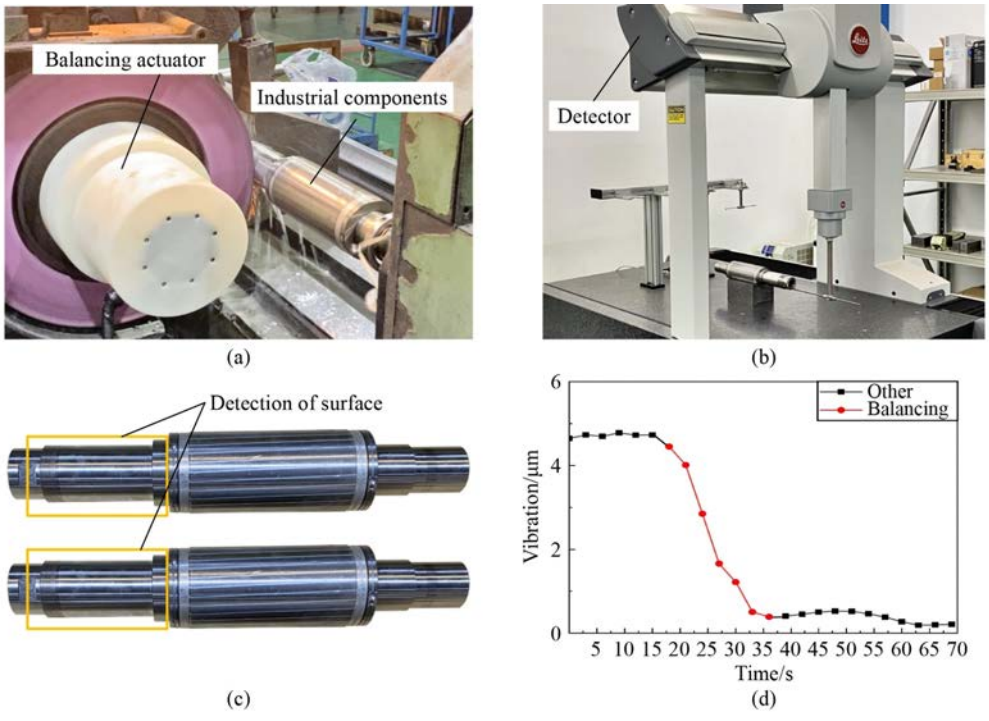

Fig. 16 Experimental results of machining workpieces: (a) processing site, (b) performance testing, (c) workpieces to be processed, and (d) unbalance vibration self-recovery regulation process.

Table 4 Comparison of surface quality of machined workpieces

Testing item	Normal working condition/mm	Install UVSRR system/mm	Upgrade/ %
Roundness 1	0.0013	0.0011	15.4
Roundness 2	0.0016	0.0010	37.5
Roundness 3	0.0015	0.0009	40.0
Roundness 4	0.0015	0.0012	20.0
Cylindricity	0.0047	0.0025	44.7
Roughness	0.3013×10^{-3}	0.2588×10^{-3}	14.1
Shape error	2.4384×10^{-3}	1.9235×10^{-3}	21.1

the machined workpieces, such as roundness and shape error, was improved by 20%–40%, and the surface quality, such as roughness, was also enhanced to a certain extent. The system achieved the purpose of extending the life of the grinding machine spindle and improving the operation accuracy.

5 Conclusions

This paper proposes a radial electromagnetic type UVSRR system for high-end grinding machine spindles. The value and technical importance of the UVSRR method are first explained, which leads to the radial electromagnetic type UVSRR system, whose working principle and system composition are described. The performance parameters of the balancing actuator, such as self-locking and driving torque, were calculated and simulated. A high-end grinding machine self-recovery regulation test bench was built to verify the balancing actuator's physical performance. Finally, a factory's universal cylindrical grinding machine was used as the experimental object to suppress the vibration of the spindle, and the operating accuracy and the grinding wheel life were improved. In future research, the structure of the balancing actuator will be further optimized, and the control method of the UVSRR system will be improved to enhance the control efficiency to provide theoretical reference and physical support for engineering applications.

Nomenclature

A_g	Effective magnetic pole area
$\boldsymbol{B}_r$	Remaining magnetic strength of the magnets
$\boldsymbol{B}_g$	Magnetic induction intensity generated by the magnets
$\boldsymbol{C}$	Damping matrix of the spindle system
$\boldsymbol{F}$	Total self-locking force
$\boldsymbol{F}_0$	Unbalance fault force on the spindle system
$\boldsymbol{F}_1$	Self-recovery force
$\boldsymbol{F}_g$	Attraction force between the magnets
$\boldsymbol{g}$	Gravitational acceleration
$\boldsymbol{G}$	Gyroscopic matrix of the spindle system
H_c	Magnetic coercivity
J	Rotational inertia of the counterweight discs and its accessories
K	Number of magnets
K_{sf}	Safety factor
$\boldsymbol{K}$	Stiffness matrix of the spindle system
m_1, m_2	Masses of the counterweight blocks 1 and 2, respectively
$\boldsymbol{m}$	Mass matrix of the balancing actuator
$\boldsymbol{M}$	Mass matrix of the spindle system
R	Mounting radius of the magnets
R_1, R_2	Center of gravity of the counterweight blocks 1 and 2, respectively
R_g	Radius of the magnet
t	Time
$\boldsymbol{T}_s$	Total self-locking torque
$\boldsymbol{T}_{sm}$	Minimum self-locking torque
$\boldsymbol{x}$	Vibration parameter of amplitude and phase of the spindle system
$\ddot{\boldsymbol{x}}$	Acceleration of the spindle system
$\boldsymbol{\alpha}$	Spindle starting acceleration
$\boldsymbol{\omega}$	Angular velocity of the spindle system
$\boldsymbol{\varphi}$	Initial phase of the spindle system
δ_2	Air gap
μ	Relative permeability
μ_0	Magnetic permeability of air

Acknowledgements This work was supported by the National Natural Science Foundation of China (Grant No. 51875031) and the Natural Science Foundation of Beijing, China (Grant No. 3212010).

Conflict of Interest The authors declare that they have no conflict of interest.

References

1. Wang J L, Xu C Q, Zhang J, Zhong R. Big Data analytics for intelligent manufacturing systems: a review. Journal of Manufacturing Systems, 2022, 62: 738–752
2. Cohen Y, Singer G. A smart process controller framework for Industry 4.0 settings. Journal of Intelligent Manufacturing, 2021, 32(7): 1975–1995
3. Gao R X, Wang L H, Helu M, Teti R. Big Data analytics for smart factories of the future. CIRP Annals-Manufacturing Technology, 2020, 69(2): 668–692
4. Kusiak A. Smart manufacturing must embrace Big Data. Nature, 2017, 544(7648): 23–25
5. Spakovszky Z S. Instabilities everywhere! Hard problems in aero-engines. Journal of Turbomachinery, 2023, 145(2): 021011

6. Hong J, Yu P C, Ma Y H, Zhang D Y. Investigation on nonlinear lateral-torsional coupled vibration of a rotor system with substantial unbalance. Chinese Journal of Aeronautics, 2020, 33(6): 1642–1660
7. Yu P C, Zhang D Y, Ma Y H, Hong J. Dynamic modeling and vibration characteristics analysis of the aero-engine dual-rotor system with fan blade out. Mechanical Systems and Signal Processing, 2018, 106(4): 158–175
8. Sinha S K. Rotordynamic analysis of asymmetric turbofan rotor due to fan blade-loss event with contact-impact rub loads. Journal of Sound and Vibration, 2013, 332(9): 2253–2283
9. Li B Q, Ma H, Yu X, Zeng T, Guo X M, Wen B C. Nonlinear vibration and dynamic stability analysis of rotor-blade system with nonlinear supports. Archive of Applied Mechanics, 2019, 89(7): 1375–1402
10. Gao J J. Artificial Self-recovery and Autonomous Health of Machine. Singapore: Springer, 2022
11. Gao J J. Bionic artificial self-recovery enables autonomous health of machine. Journal of Bionics Engineering, 2022, 19(6): 1545–1561
12. Gao J J. A study of the fault self-recovery regulation for process equipment. In: Proceedings of International Conference on Intelligent Maintenance Systems. Xi'an, 2003, 779–786 (in Chinese)
13. Gao J J. Artificial self-recovery and machinery self-recovery regulation system. Journal of Mechanical Engineering, 2018, 54(8): 83–94
14. Cao H R, Zhang X W, Chen X F. The concept and progress of intelligent spindles: a review. International Journal of Machine Tools and Manufacture, 2017, 112: 21–52
15. Jin H H, Miller G M, Pety S J, Griffin A S, Stradley D S, Roach D, Sottos N R, White S R. Fracture behavior of a self-healing, toughened epoxy adhesive. International Journal of Adhesion and Adhesives, 2013, 44: 157–165
16. Casavola A, Rodrigues M, Theilliol D. Self-healing control architectures and design methodologies for linear parameter varying systems. International Journal of Robust and Nonlinear Control, 2015, 25(5): 625–626
17. Li H, Wang F L, Li H R. Abnormal condition identification and self-healing control scheme for the electro-fused magnesia smelting process. Acta Automatica Sinica, 2020, 46(7): 1411–1419 (in Chinese)
18. Chen F Y, Jiang B, Tao G. Direct self-repairing control for helicopter via quantum control and adaptive compensator. Transactions of Nanjing University of Aeronautics and Astronautics, 2011, 28(4): 337–342
19. Pan X, He X T, Wu H Q, Ju C L, Jiang Z N, Gao J J. Optimal design of novel electromagnetic-ring active balancing actuator with radial excitation. Chinese Journal of Mechanical Engineering, 2021, 34(1): 9
20. Pan X, Lu J Q, Huo J J, Gao J J, Wu H Q. A review on self-recovery regulation (SR) technique for unbalance vibration of high-end equipment. Chinese Journal of Mechanical Engineering, 2020, 33(1): 89
21. Li Z J, Chen L F, Zhou B, Yan Z W, Zhou S H. Magnetic circuit optimization and experimental study of new internally excited automatic balancing. High Technology Letters, 2021, 27(2): 173–183
22. Yao J F, Yang F Y, Su Y F, Scarpa F, Gao J J. Balancing optimization of a multiple speeds flexible rotor. Journal of Sound and Vibration, 2020, 480: 115405
23. Ranjan G, Tiwari R. On-site high-speed balancing of flexible rotor-bearing system using virtual trial unbalances at slow run. International Journal of Mechanical Sciences, 2020, 183: 105786
24. Hredzak B, Guo G X. New electromechanical balancing device for active imbalance compensation. Journal of Sound and Vibration, 2006, 294(4–5): 737–751
25. Li X G, Zhao C H, Feng Q, Zhou Y, ZHOU H, Jiang C M, Liu B Y, Xu M, Sun Y X. CN Patent, 205138714, 2016-04-06
26. Kume H, Hibi T, Sogawa T. US Patent, 6219328B1, 2001-04-17
27. Zhang X N, Liu X, Zhao H. New active online balancing method for grinding wheel using liquid injection and free dripping. Journal of Vibration and Acoustics, 2018, 140(3): 031001
28. Urbiola-Soto L, Lopez-Parra M, Cuenca-Jimenez F. Improved design of a bladed hydraulic balance ring. Journal of Sound and Vibration, 2014, 333(3): 669–682
29. Langthjem M A, Nakamura T. Highly nonlinear liquid surface waves in the dynamics of the fluid balancer. Procedia IUTAM, 2016, 19: 110–117
30. Fan H W, Jing M Q, Wang R C, Liu H, Zhi J J. New electromagnetic ring balancer for active imbalance compensation of rotating machinery. Journal of Sound and Vibration, 2014, 333(17): 3837–3858
31. Moon J D, Kim B S, Lee S H. Development of the active balancing device for high-speed spindle system using influence coefficients. International Journal of Machine Tools and Manufacture, 2006, 46(9): 978–987
32. Pan X, Peng R X, Zhang H Y, Wu H Q, Gao J J. Research on new electromagnetic type automatic balancing system for high-end machinery and equipment. Journal of Mechanical Engineering, 2022, 58: 1–10 (in Chinese)
33. LORD Corporation. US Patent, 8961139B2, 2015-02-24
34. Hofmann Maschinen-und Anlagenbau GmbH. US Patent, 8875572B2, 2014-11-04
35. ARICHELL Technologies. CA Patent, 2538524C, 2015-09-08
36. Zhu C S, Wang X X. Vibration control of advanced hybrid squeeze film damper on a flexible rotor system. Journal of Mechanical Engineering, 1996, 32(3): 76–83 (in Chinese)
37. Zeng S, Wang X X, Li Y Y. Research on unbalance identification method of double rotors system with slightly different rotating speed. Journal of Vibration Engineering, 1996, 9(4): 399–404 (in Chinese)
38. Pan X, Wu H Q, Jiang Z N, Gao J J. US Patent, 11362565B2, 2022-06-14